applied sciences

MDPI

Article

Design of a 90 GHz SOI Fin Electro-Optic Modulator for High-Speed Applications

Hany Mahrous [1], Mostafa Fedawy [1], Mona El Sabbagh [2], W. Fikry [2] and Michael Gad [2,*]

[1] Electronics and Communications Department, Faculty of Engineering, Arab Academy for Science and Technology and Maritime Transport, Cairo 2033, Egypt; h.a.mahmod@gmail.com (H.M.); m.fedawy@aast.edu (M.F.)

[2] Engineering Physics and Mathematics Department, Faculty of Engineering, Ain Shams University, Cairo 11517, Egypt; mona.mohammed@eng.asu.edu.eg (M.E.S.); wael_fikry@eng.asu.edu.eg (W.F.)

* Correspondence: mmonirmo@eng.asu.edu.eg

Received: 29 August 2019; Accepted: 12 November 2019; Published: 15 November 2019

Abstract: Introducing high speed networks, such as the fifth generation of mobile technology and related applications including the internet of things, creates a pressing demand for hardware infrastructure that provides sufficient bandwidth. Here, silicon-based microwave-photonics presents a solution that features easy and inexpensive fabrication through a mature platform that has long served the electronics industry. In this work, the design of an electro-optic modulator is proposed where the 'fin' structure is adopted from the domain of electronics devices, with emphasis on the high speed of operation. The proposed modulator is customized to provide a bandwidth of 90 GHz with a small phase shifter length of 800 µm and an optical insertion loss of 4 dB. With such a speed, this proposed modulator fits high-speed applications such as modern tele-communications systems.

Keywords: CMOS; integrated optics; silicon photonics; modulators

1. Introduction

Optical interconnects demonstrate core advantages over their traditional electrical counterparts in many aspects such as immunity to electromagnetic interference, high data transfer rates, and low losses [1,2]. Having integrated systems with such characteristics will be also very advantageous if the systems are complementary metal-oxide semiconductor (CMOS) compatible. Such compatibility adds compactness, low-cost and ease of fabrication to the previous list of advantages. This concept gave a big momentum for silicon photonics for almost three decades. Currently, with many components being mature enough [3–12], silicon photonics stands ready to serve in many speed-demanding applications, such as 5G networks [13], central processing unit (CPU)–memory interconnects [14] and radio-over-fiber (RoF) [15]. A key device in such applications is the electro-optic modulator where electrical data converts into optical data [16], before commencing its trip over low-loss optical fibers.

The main method to modulate laser in a silicon waveguide is the plasma dispersion effect which was quantitatively described by Soref about three decades ago [17]. This technique is the practical way to get around the small electro-optic coefficient of silicon. In this method, the modulating voltage manipulates the charge carrier concentration in doped silicon. The result is the variation of both parts of the effective refractive index, the real, n_e, which is responsible for the mode phase shift and the imaginary, k, which is responsible for the optical power loss. Based on this idea, two families of modulators can be studied. The first family, which includes carrier-injection modulators, is the one that grabbed attention earlier. Here, electric current flows through the waveguide leading to an increase in the charge concentration, which decreases n_e but increases k. Although this current flow results in a big change in n_e and hence enables a relatively short phase shifter length, the speed is limited

because of the carrier recombination time [18–20]. Another drawback is the DC power consumption. The second family, which includes carrier-depletion modulators, is a more successful one. In this approach, usually a reverse-biased PN junction is positioned within the phase shifter [21]. With the reverse bias, the junction works as a voltage-controlled capacitor. The concentration of the carriers changes between two states, where recombination does not take place in any. This way, the device 3-dB bandwidth $f_{3\text{dB}} = \frac{1}{2\pi RC}$ is limited by the junction capacitance, C, and the circuitry resistance, R. Hence, higher speeds can be achieved. There is also zero DC power consumption in this technique. An extensive work was invested in this direction, where different PN junction-based structures were introduced to maximize the interaction between the optical mode and the junction [22–24]. However, the depletion cannot be increased arbitrarily because of the silicon breakdown limit, a fact that sets a limit to the modulation efficiency [25]. This approach can also make use of metal-oxide semiconductor (MOS) devices [26]. Here, not only depletion can be utilized, but also accumulation of charge. One of these two modes of operation can be used, or even both, to create a larger contrast of n_e and hence minimize the phase shifter length. Unfortunately, the inversion mode is not useful at high frequencies of operation [26]. In MOS based modulators, the modulator speed can be limited if the oxide thickness is small [25]. Besides, having a small oxide thickness might result in high optical insertion loss if the metallic electrodes come close enough to the optical mode. The only benefit of a thin oxide layer is the low modulating voltage.

Apart from silicon modulation using plasma dispersion, different alternatives were suggested. In one alternative, silicon can be thermally modulated since it has a high thermo-optic coefficient of 1.8×10^{-4} K^{-1} . However the modulation speed is very limited [27]. In another alternative, silicon is covered with a cladding material which possesses a much stronger electro-optic coefficient [28–30]. The cladding material modulates the part of the mode that overlaps with it. Other platforms such as polymers [31], III-V semiconductors [32,33] and graphene [34–36] were also proposed. However, it is always advantageous to stick to the silicon-on-silica platform to keep fabrication simplicity and low cost.

In this work, a MOS based modulator is proposed. The structure utilizes the fin-gate structure which is widely used as a part of the field effect transistor (FET) [37–39]. The proposed design has a main target of providing the maximum possible speed in order to make this modulator a candidate for the bandwidth aggressive applications, like those mentioned above. Such applications require speeds, for example, more than 100 Gbps of non-return-to-zero (NRZ) code [13]. Other design targets are small size and low optical losses. Finally, the design is confined to the mature silicon-on-silica platform which guarantees possible future implementation at low-cost.

2. Modulator Structure and the Performance Parameters

A cross section of the phase shifter is shown in Figure 1a. The shifter consists of a rectangular waveguide of silicon core and silicon dioxide cladding. The width of the core is W and its height is H. Three rectangular pieces of aluminum are placed around the core to form the electrodes. The top and right pieces are electrically connected to the modulating voltage while the left is grounded. The silica layer between the core and the right or left electrodes has a thickness denoted by y_o. A silica layer of thickness z_o separates the core from the top electrode.

The proposed modulator employs the Mach–Zender interferometer (MZI) structure where light propagates through two arms, as shown in Figure 1b. Each arm possesses a phase-shifter as the one just described. When the applied modulating voltage, V, is zero on both arms, the two modes in the MZI arms are in phase and the output power is high, P_H. Applying a voltage difference to the arms, the output optical power is then low, P_L. The extinction ratio, ER, in dB is given by $ER = 10 \log \frac{P_H}{P_L}$ [40]. If the input optical power is P_o, then the insertion loss, IL, in dB is given by $IL = 10 \log \frac{P_o}{P_H}$. One goal in such designs is to maximize ER and minimize IL. The voltage difference is applied to the arms in the form of positive voltage, V_1, on one arm and negative voltage, V_2, on the other. This technique is known as the push–pull technique [41] and is useful to decrease the voltage applied to an arm.

See Figure 1b. The phase shifter length is denoted by L. If this length is enough to produce a π phase-shift between the two arms, then the length is called the 'effective length', denoted by L_π. This length is calculated from $L_\pi = \frac{\lambda_o}{2\Delta n_e}$, where λ_o is the free-space wavelength of the light and Δn_e is the difference in the effective index, Δn_e, between the propagating modes in the two arms. The required voltage difference to induce this phase shift is denoted by V_π. In such a case, ER is at its absolute maximum since P_L is at its absolute minimum. The reason for why P_L cannot go down to zero is that the two arms do not possess the same optical loss, since the optical loss due to plasma dispersion is function of the applied voltage, which inherently is not the same for the two arms. Hence, ER cannot be infinity. Still, due to small differences in the optical loss values in the two arms and also due to the short arm length, very high ER values can be achieved as will be discussed later. A trade-off exists, on the other hand, between the aforementioned parameters. The device size can be reduced, to enable higher fabrication density, lower IL, and lower C and hence higher $f_{3\text{dB}}$, at the expense of the phase shift between the arms, which results in a decrease in ER.

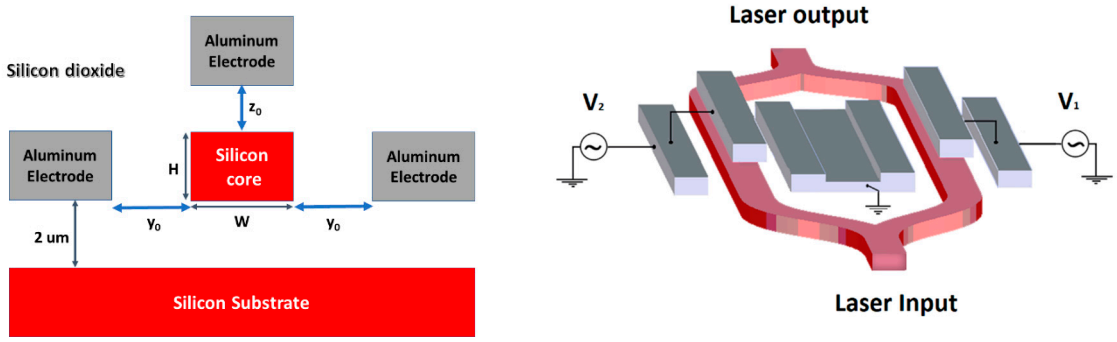

(**a**) (**b**)

Figure 1. (**a**) A cross section of the phase shifter. The silicon core is separated from the silicon substrate by a buried oxide layer that is 2 µm thick. (**b**) Three-dimensional view of the proposed MZI modulator.

3. Optimizing the Modulator Parameters

In this section, the dimensions of the waveguide cross section, the silica thickness and the core doping, are optimized in order to achieve the best performance of the modulator in terms of losses, speed and size. In this work, the mode profile and the effective index are found using the commercially available software, MODE, while the plasma dispersion is simulated using DEVICE, both from Lumerical [42]. The simulation settings are shown in Appendix A. Three waveguide cross sections are tested. The heights are taken as $H = 150$ nm, 220 nm, and 300 nm with the corresponding width values $W = 600$ nm, 450 nm, and 400 nm, respectively. Those dimensions ensure single mode operation at $\lambda_o = 1.55$ µm. The mode of interest in this work is the transverse electric field like (TE-like) mode which has its major electric field component parallel to the substrate. The electric field intensity, for the mode supported by each of the three different waveguides, is shown in Figure 2. In this design, acceptors are chosen for the doping, since holes have a stronger effect on the change of n_e than electrons [17]. The doping concentration, N_A, is varied from 1×10^{16} cm^{-3} to 3×10^{17}cm^{-3}. For each value of N_A, the values of y_o and z_o are swept from 200 nm to 500 nm in steps of 100 nm while the value of the modulating voltage, V, is swept from −20 Volt to 20 Volt in steps of 1 Volt.

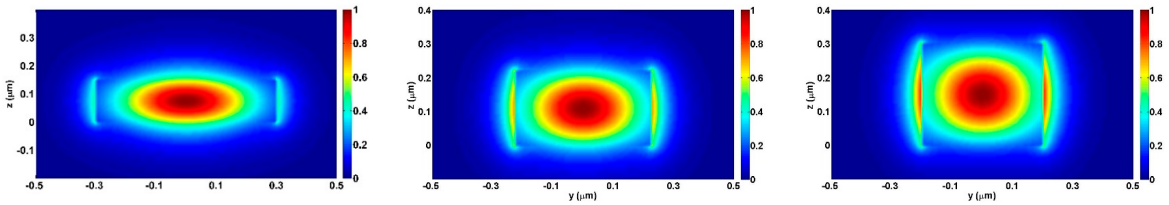

(**a**) (**b**) (**c**)

Figure 2. Electric field intensity distribution over the cross section of a waveguide with (**a**) $H = 150$ nm and $W = 600$ nm, (**b**) $H = 220$ nm and $W = 450$ nm, and (**c**) $H = 300$ nm and $W = 400$ nm. The buried oxide layer lies below $z = 0$.

The insertion loss for this device comprises four mechanisms. Three loss mechanisms are related to the propagation through the waveguide. First, the free carrier absorption loss, which depends on N_A and V. Second, the optical absorption due to the overlap between the optical mode and the metallic electrodes. The total of the two losses is found through DEVICE and MODE simulations, in dB/cm, and is given the symbol α_o. Third, the passive waveguide scattering losses, taken here as 1 dB/cm [43]. This loss is to be added to α_o to give the total phase shifter loss, which is designated by α, in dB/cm . The fourth loss mechanism is the insertion loss due to the two Y-junctions of the MZI, which is taken here as 0.3 dB for each junction, totalling 0.6 dB of optical losses for the MZI [44].

With all of the dimensions and the doping dose combinations, a selection criterion is necessary to pick the desired device. First, the results are filtered for the smallest IL at each doping concentration when $V = 0$. This selection criterion simply picks the configurations with maximum silica thickness in the range of this study, $y_o = z_o = 500$ nm, because the overlap of optical mode with the electrodes is minimal. According to this criterion, the phase shifter loss, αL, when $L = L_\pi$, is plotted versus the doping concentration in Figure 3a. In Figure 3b, the corresponding effective length, L_π, is plotted versus the doping concentration.

The first remark here is that the waveguide with $H = 300$ nm, which has the largest cross-sectional area, is the one that shows the largest L_π at all concentrations. This finding follows from the fact that a larger cross section means more charge resides inside the phase shifter. Hence, manipulating the charge density with the modulating voltage is less effective. This results in a smaller change of the effective index and consequently a longer L_π.

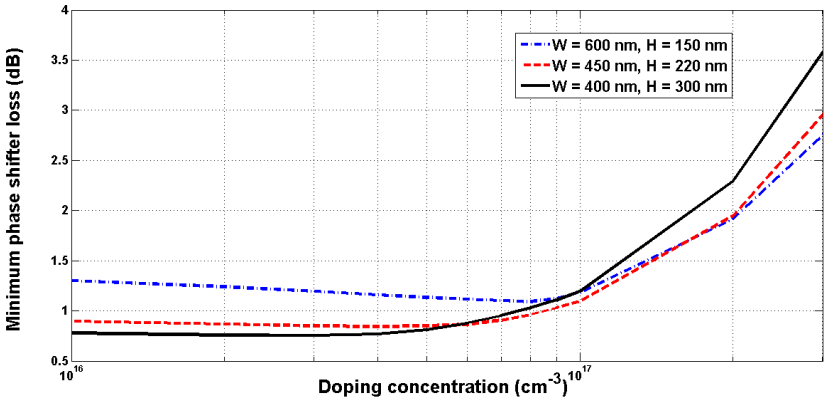

(**a**)

Figure 3. *Cont.*

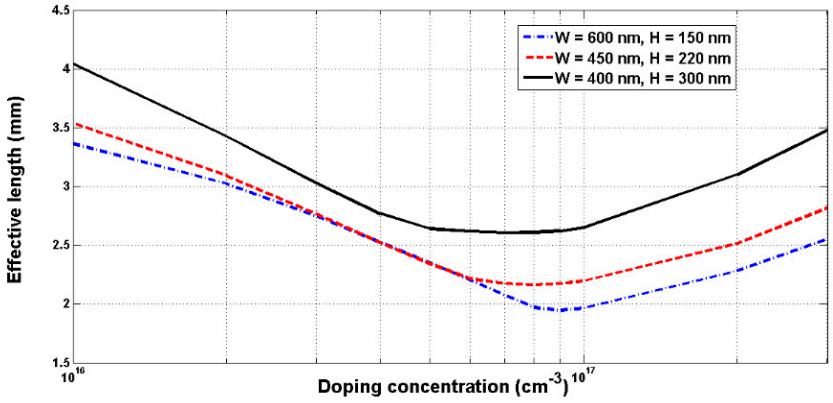

(**b**)

Figure 3. (**a**) Minimum phase shifter loss versus the doping concentration. (**b**) Corresponding effective length versus the doping concentration.

The second remark is that the waveguide with the largest H exhibits the lowest optical losses at low levels of doping concentrations, despite the previous finding. This can be explained by the small carrier absorption loss which allows the electrode absorption to be the dominant loss. Using MODE, the waveguide with $H = 300$ nm has a confinement factor, defined as the ratio of the core power to the total mode power, $\Gamma = 84\%$. This is the largest amongst the three and hence its mode has the least overlap with the electrodes at the same y_o and z_o. The waveguide with $H = 220$ nm has $\Gamma = 77\%$ and the one with $H = 150$ nm has $\Gamma = 60\%$. However, as the doping dose increases, apparently, the carrier absorption loss becomes the dominant and hence the waveguide with $H = 300$ nm becomes the most lossy.

Based on the previous discussion, the device that shows the lowest IL is found from Figure 3a, as the one with $H = 300$ nm, $W = 400$ nm, $L = L_\pi = 3$ mm, $N_A = 3 \times 10^{16}$ cm^{-3}, $IL = 0.75 + 0.6 = 1.35$ dB. The other parameters for this design are $V_\pi = 30$ Volt and $ER = 29.5$ dB. Using DEVICE, we find the capacitance per micrometer of the propagation path, $C' = 0.04 \frac{fF}{\mu m}$. Then, the total device capacitance $C = C'L = 121\ fF$ which gives $f_{3\text{dB}} = \frac{1}{2\pi RC} = 26$ GHz. Note that in the bandwidth calculations we employ the commonly used value of contact resistance $R = 50\ \Omega$. This design shows a small IL and a very high ER. This device is referred to as 'Modulator A' in the next discussion.

Next, the selection criterion could be altered to target a higher speed of modulation, at the expense of the insertion loss. With closer electrodes at $z_o = 300$ nm and $y_o = 500$ nm and for $H = 150$ nm, $W = 600$ nm and $N_A = 2 \times 10^{17}$cm^{-3} we get $L_\pi = 1.6$ mm, $IL = 6.9 + 0.6 = 7.5$ dB, $ER = 26.7$ dB $V_\pi = 40$ Volt, $C' = 0.044 \frac{fF}{\mu m}$, and $f_{3\text{dB}} = 44$ GHz. This interesting case has its main device parameters shown in Figure 4. As the modulating voltage, V, increases above zero, the holes deplete and therefore the effective index increases and the phase shifter loss decreases [17]. With depletion, the capacitance decreases in value since the charge inside the silicon waveguide moves away from the silicon edges which effectively enlarges the capacitor width [45]. With negative V, the hole concentration increases which results in a decrease in n_e and increase in α_o. The charge accumulating at the silicon edge makes the effective thickness of the capacitor determined by the oxide thickness [45]. Therefore, the capacitance is higher in the accumulation regime. To account for the slowest response, this value is used in the 3-dB bandwidth calculations, although the maximum change of the capacitance is approximately 2% over the entire range of the modulating voltage.

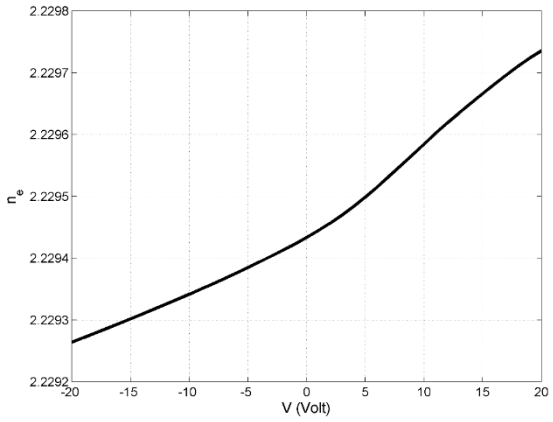

(**a**)

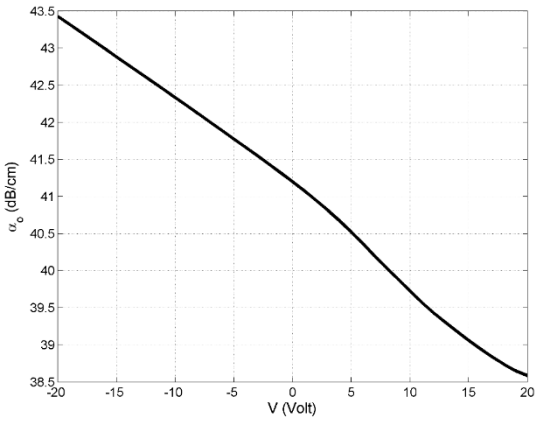

(**b**)

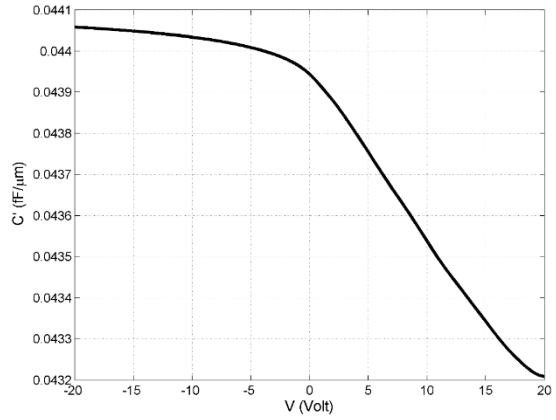

(**c**)

Figure 4. Effect of the modulating voltage on (**a**) the effective refractive index, (**b**) the phase shifter loss, and (**c**) the capacitance per unit length, for 'Modulator B'.

Then, a modification can be adopted to push the speed up. By shortening the phase shifter length to $L = 0.8$ mm $= 800$ μm, the speed goes up to 90 GHz, the insertion loss goes down to

$IL = 3.4 + 0.6 = 4$ dB while the extinction ratio decreases to $ER = 3$ dB. Although being much smaller, this ER value is widely reported in literature as an acceptable value [22,46–50]. This design is referred to as 'Modulator B'.

A third alternative is a design with low modulation voltage. We find that the device with $H = 150$ nm, $W = 600$ nm, $N_A = 10^{16}$ cm^{-3}, $z_o = 400$ nm, $y_o = 500$ nm has the following: $V_\pi = 22$ Volt, $L_\pi = 3$ mm, $IL = 3 + 0.6 = 3.6$ dB, $ER = 28$ dB, $f_{3\text{dB}} = 24$ GHz. The depletion reaches its maximum when the applied voltage to one arm is 2 *Volt* only. The rest of the V_π which is 20 Volt are employed in the accumulation regime for the other arm. Seeking a low voltage of operation, this device can be operated between $V = 0$ and $V = 2$ Volt, sacrificing the accumulation contribution to Δn_e. Along with $L = 7.5$ mm, we get $IL = 7.5 + 0.6 = 8.1$ dB, $ER = 3$ dB, and $f_{3\text{dB}} = 10$ GHz. This design is called 'Modulator C'.

Looking into the former range of results, 'Modulator B', with $f_{3\text{dB}} = 90$ GHz, can be employed in the backhaul truck circuits of the 5G networks with a speed of 100 Gbps of non-return-to-zero (*NRZ*) coding [13], where also high voltage can be provided. 'Modulator C', which exhibits much lower bandwidth but also much lower voltage of operation, is then more suitable for the end user applications of the 5G systems where the speed of operation is 1–10 Gbps [13], which can be easily supported by a bandwidth of 10 GHz. A summary of the proposed variants of this modulator is given in Table 1.

Table 1. Summary of the proposed structures.

Modulator	Main Feature	$V_\pi L_\pi$ (Volt.cm)	Voltage (Volt)	L (mm)	3 dB Bandwidth (GHz)	*IL* (dB)	*ER* (dB)
A	Low *IL* and high *ER*	9	30	3	26	1.35	29.5
B	High speed	6.4	40	0.8	90	4	3
C	Low voltage	6.6	2	7.5	10	8.1	3

4. Comparison with Other Devices

Many modulator structures have been proposed in the literature. The most important of which are summarized in Table 2.

Table 2. Summary of previously published designs.

Reference	Structure	$V_\pi L_\pi$ (Volt.cm)	V (Volt)	L (mm)	Speed * (Gbps)	*IL* (dB)	*ER* (dB)
[51]	MOS	–	25	0.11–0.15	–	5–10	–
[52]	MOS	8	3.5	2.5 10	1	– 6.7	– 16
[53]	MOS	8	3.5	2.5	2.5 1	5.1 6.7	5 –
[26]	MOS	–	30	14	19	9–25	–
[46]	MOS	3.3	1.4	3.45	10	10	3.8
[54]	MOS	24	30	8	0.02	–	0.6
[55]	MOS	0.3	1.5	0.2	15	2.2	3.6
[56]	MOS	0.3	2.5	–	10	4	5
[57]	MOS	0.5	2	2.5	–	5	–
[50]	MOS	1.53	6	0.5	25	26	3.65
[58]	PN Junction	4	6	1	40	4	1.1
[48]	PN Junction	2.7	4	3.5	40	15	10
[59]	Wrapped around PN Junction	11	6	1.3	40	25	6.5
[22]	PIPIN Junction	3.5	7	4.7	20	6	6.6
[60]	PN Junction+ slow light structure	0.85	1	0.5	40	11	8.5
[61]	PN Junction	2	2.7	0.75	60	3.5	4.4

– Data is not available. * The speed is related to the 3 dB bandwidth using the relation Speed $= 2 \times$ (3 dB bandwidth), where the non-return-to-zero modulation is assumed.

Looking into the previous performance metrics, the proposed modulator in this work features the simplest fabrication process, especially if compared to complicated PN junction designs in [20] and [46]. The reason is that this modulator is based on the 'fin' structure which is a standard structure in the electronics industry. This feature enables easy and inexpensive fabrication of the proposed modulator through, for example, the multi-project-wafer (MPW) prototyping service from IMEC [62]. 'Modulator B' features a very high bandwidth of 90 GHz which can accommodate up to 180 Gbps of

NRZ signal. Also, it possesses a competitive phase shifter length and an acceptable insertion loss and extinction ratio, compared to the modulators in Table 2. However, with the high voltage of operation, this modulator is more suitable for backbone circuits. For the end user device, the alternative is given as 'Modulator C'.

5. Conclusions

In this work, a MOS-based modulator has been proposed. The modulator employs a standard structure from the electronics domain, the 'fin' gate structure. This makes the modulator easy and inexpensive to fabricate. We showed how the design parameters—such as the doping concentration, the waveguide dimensions, and the silica thickness—can be altered to get different variants of the proposed modulators. The performance metrics such as the insertion loss, the extinction ratio, the modulation speed and the voltage of operation can then be customized to make the modulator suitable at different points of a communications network. The very high bandwidth of 90 GHz is introduced to match the 5G network requirements at the backhaul truck. This way, silicon photonics can be easily integrated with the prospective networks for high speed communications and the internet of things.

Author Contributions: Conceptualization, M.G. and M.F.; Methodology, H.M., M.G., and M.F.; Software, H.M. and M.E.S.; Validation, M.G., M.F., and W.F.; Formal analysis, H.M. and M.G.; Investigation, H.M.; Resources, M.G. and M.F.; Data curation, H.M. and M.G.; Writing—original draft preparation, H.M. and M.G.; Writing—review and editing, M.G., M.F., M.E.S., and W.F.; Visualization, H.M.; Supervision, W.F.; Project administration, M.G. and M.F.

Funding: This research received no external funding.

Conflicts of Interest: The authors declare no conflict of interest.

Appendix A

The simulation settings in this work are:

Device:

Simulation window	2*D x − normal* & $y = 4$ μm & $z = 2$ μm
Mesh Size	Minimum edge length = 5 nm & Maximum edge length = 100 nm
Temperature	300 K
Temperature Dependence	Isothermal
Material Parameters	
Silicon	Permittivity = 11.7 & Work function = 4.59 eV & $ni = 1.5e10$
Mobility physical models	Auger Radiative trap-assisted (SRH)
Oxide SiO2	Permittivity = 3.9
Aluminum	work function = 4.28 eV

MODE:

Simulation window:	2D x-normal & $y = 4$ μm & $z = 2$ μm
Temperature:	300 K
Mesh:	5 nm inside the core & 10 nm elsewhere
Boundary conditions:	PML
Wavelength:	1.55 um

References

1. Chen, Y.; Kibune, M.; Toda, A.; Hayakawa, A.; Akiyama, T.; Sekiguchi, S.; Ebe, H.; Imaizumi, N.; Akahoshi, T.; Akiyama, S.; et al. A 25Gb/s hybrid integrated silicon photonic transceiver in 28nm CMOS and SOI. In Proceedings of the 2015 IEEE International Solid-State Circuits Conference—(ISSCC) Digest of Technical Papers, San Francisco, CA, USA, 22–26 February 2015; Volume 58, pp. 402–403.
2. Waterhouse, R.; Novack, D. Realizing 5G: Microwave Photonics for 5G Mobile Wireless Systems. *IEEE Microw. Mag.* **2015**, *16*, 84–92. [CrossRef]
3. Gad, M.; Zaki, A.; Sabry, Y.M. Silicon photonic mid-infrared grating coupler based on silicon-on-insulator technology. In Proceedings of the 2017 34th National Radio Science Conference (NRSC), Alexandria, Egypt, 13–16 March 2017; pp. 400–406.
4. Halir, R.; Ortega-Moñux, A.; Schmid, J.H.; Alonso-Ramos, C.; Lapointe, J.; Xu, D.X.; Wangüemert-Pérez, J.G.; Molina-Fernández, Í.; Janz, S. Recent advances in silicon waveguide devices using sub-wavelength gratings. *IEEE J. Sel. Top. Quantum Electron.* **2013**, *20*, 279–291. [CrossRef]
5. Barrios, C.A. Integrated microring resonator sensor arrays for labs-on-chips. *Anal. Bioanal. Chem.* **2012**, *403*, 1467–1475. [CrossRef] [PubMed]
6. Gad, M.; Yevick, D.; Jessop, P. A comparison of modeling methods for ring resonator circuits. *J. Opt. Soc. Am. A* **2010**, *27*, 703. [CrossRef] [PubMed]
7. Van Member, V.; Ibrahim, T.A.; Absil, P.P.; Johnson, F.G.; Grover, R.; Ho, P.T. Optical signal processing using nonlinear semiconductor microring resonators. *IEEE J. Sel. Top. Quantum Electron.* **2002**, *8*, 705–713.
8. Brooks, C. Passive silicon-on-insulator polarization-rotating waveguides. *Opt. Eng.* **2006**, *45*, 044603. [CrossRef]
9. Gad, M.; Yevick, D.; Jessop, P. High sensitivity ring resonator gyroscopes. *Fiber Integr. Opt.* **2011**, *30*, 395–410.
10. Bharti, G.K.; Rakshit, J.K. Design and Performance Analysis of High Speed Optical Binary Code Converter using Micro-Ring Resonator. *Fiber Integr. Opt.* **2018**, *37*, 103–121. [CrossRef]
11. Gobert, O.; Rovera, D.; Mennerat, G.; Comte, M. Linear Electro Optic Effect for High Repetition Rate Carrier Envelope Phase Control of Ultra Short Laser Pulses. *Appl. Sci.* **2013**, *3*, 168–188. [CrossRef]
12. Marchetti, R.; Vitali, V.; Lacava, C.; Cristiani, I.; Giuliani, G.; Muffato, V.; Fournier, M.; Abrate, S.; Gaudino, R.; Temporiti, E.; et al. Low-loss micro-resonator filters fabricated in silicon by CMOS-compatible lithographic techniques: Design and characterization. *Appl. Sci.* **2017**, *7*, 174. [CrossRef]
13. Alavi, S.E.; Soltanian, M.R.K.; Amiri, I.S.; Khalily, M.; Supa'at, A.S.M.; Ahmad, H. Towards 5G: A Photonic Based Millimeter Wave Signal Generation for Applying in 5G Access Fronthaul. *Sci. Rep.* **2016**, *6*, 19891. [CrossRef] [PubMed]
14. He, H.; Liu, F.; Li, B.; Xue, H.; Wang, H.; Qiu, D.; Zhou, Y.; Cao, L. Research on Optical Transmitter and Receiver Module Used for High-Speed Interconnection between CPU and Memory. *Fiber Integr. Opt.* **2016**, *35*, 212–229. [CrossRef]
15. Wake, D.; Nkansah, A.; Gomes, N.J. Radio over fiber link design for next generation wireless systems. *J. Light. Technol.* **2010**, *28*, 2456–2464. [CrossRef]
16. Liu, K.; Ye, C.R.; Khan, S.; Sorger, V.J. Review and perspective on ultrafast wavelength-size electro-optic modulators. *Laser Photonics Rev.* **2015**, *9*, 172–194. [CrossRef]
17. Soref, R.A.; Bennett, B.R. Electrooptical effects in silicon. *IEEE J. Quantum Electron.* **1987**, *23*, 123–129. [CrossRef]
18. Watts, M.R.; Zortman, W.A.; Trotter, D.C.; Young, R.W.; Lentine, A.L. Low-voltage, compact, depletion-mode, silicon MachZehnder modulator. *IEEE J. Sel. Top. Quantum Electron.* **2010**, *16*, 159–164. [CrossRef]
19. Barrios, C.A.; Almeida, V.R.; Panepucci, R.; Lipson, M. Electrooptic Modulation of Silicon-on-Insulator Submicrometer-Size Waveguide Devices. *J. Lightwave Technol.* **2003**, *21*, 2332–2339. [CrossRef]
20. Akiyama, S.; Kurahashi, T.; Baba, T.; Hatori, N.; Usuki, T.; Yamamoto, T. A 1 v peak-to-peak driven 10-Gbps slow-light silicon Mach-Zehnder modulator using cascaded ring resonators. *Appl. Phys. Express* **2010**, *3*, 072202. [CrossRef]
21. Gardes, F.Y.; Reed, G.T.; Emerson, N.G.; Png, C.E. A sub-micron depletion-type photonic modulator in Silicon on Insulator. *Opt. Express* **2005**, *13*, 8845. [CrossRef]
22. Ziebell, M.; Marris-Morini, D.; Rasigade, G.; Fédéli, J.-M.; Crozat, P.; Cassan, E.; Bouville, D.; Vivien, L. 40 Gbit/s low-loss silicon optical modulator based on a pipin diode. *Opt. Express* **2012**, *20*, 10591. [CrossRef]

23. Xu, H.; Xiao, X.; Li, X.; Hu, Y.; Li, Z.; Chu, T.; Yu, Y.; Yu, J. High speed silicon Mach-Zehnder modulator based on interleaved PN junctions. *Opt. Express* **2012**, *20*, 15093–15099. [CrossRef] [PubMed]
24. Pantouvaki, M.; Bogaerts, W.; Korn, D.; Alloatti, L.; Baets, R.; Hillerkuss, D.; Dumon, P.; Yu, H.; Komorowska, K.; Verheyen, P.; et al. Performance tradeoff between lateral and interdigitated doping patterns for high speed carrier-depletion based silicon modulators. *Opt. Express* **2012**, *20*, 12926.
25. Dong, P.; Chen, L.; Chen, Y. High-speed low-voltage single-drive push-pull silicon Mach-Zehnder modulators. *Opt. Express* **2012**, *20*, 6163. [CrossRef] [PubMed]
26. Barrios, C.A.; Lipson, M. Modeling and analysis of high-speed electro-optic modulation in high confinement silicon waveguides using metal-oxide-semiconductor configuration. *J. Appl. Phys.* **2004**, *96*, 6008–6015. [CrossRef]
27. Harris, N.C.; Ma, Y.; Mower, J.; Baehr-Jones, T.; Englund, D.; Hochberg, M.; Galland, C. Efficient, compact and low loss thermo-optic phase shifter in silicon. *Opt. Express* **2014**, *22*, 10487–10493. [CrossRef]
28. Gad, M.; Yevick, D.; Jessop, P.E. Tunable polymer/silicon over insulator ring resonators. *Opt. Eng.* **2008**, *47*, 124601.
29. Gan, X.; Shiue, R.J.; Gao, Y.; Meric, I.; Heinz, T.F.; Shepard, K.; Hone, J.; Assefa, S.; Englund, D. Chip-integrated ultrafast graphene photodetector with high responsivity. *Nat. Photonics* **2013**, *7*, 883–887. [CrossRef]
30. Alloatti, L.; Palmer, R.; Diebold, S.; Pahl, K.P.; Chen, B.; Dinu, R.; Fournier, M.; Fedeli, J.M.; Zwick, T.; Freude, W.; et al. 100 GHz silicon-organic hybrid modulator. *Light Sci. Appl.* **2014**, *3*, 5–8. [CrossRef]
31. Bechtel, J.H.; Menders, J.; Zang, D. Electro-optic polymer integrated optic devices and future applications. *Fiber Integr. Opt.* **2003**, *22*, 211–244. [CrossRef]
32. Bennett, B.R.; Soref, R.A.; Del Alamo, J.A. Carrier-Induced Change in Refractive Index of InP, GaAs, and InGaAsP. *IEEE J. Quantum Electron.* **1990**, *26*, 113–122. [CrossRef]
33. Tran, M.A.; Huang, D.; Komljenovic, T.; Peters, J.; Malik, A.; Bowers, J.E. Ultra-low-loss silicon waveguides for heterogeneously integrated silicon/III-V photonics. *Appl. Sci.* **2018**, *8*, 1139. [CrossRef]
34. Liu, G.-D.; Zhai, X.; Xia, S.-X.; Lin, Q.; Zhao, C.-J.; Wang, L.-L. Toroidal resonance based optical modulator employing hybrid graphene-dielectric metasurface. *Opt. Express* **2017**, *25*, 26045. [CrossRef] [PubMed]
35. Zou, X.; Zhang, Y.; Li, Z.; Yang, Y.; Zhang, S.; Zhang, Z.; Zhang, Y.; Liu, Y. Polarization-insensitive phase modulators based on an embedded silicon-graphene-siliconwaveguide. *Appl. Sci.* **2019**, *9*, 429. [CrossRef]
36. Lin, I.-T.; Lai, Y.-P.; Wu, K.-H.; Liu, J.-M. Terahertz Optoelectronic Property of Graphene: Substrate-Induced Effects on Plasmonic Characteristics. *Appl. Sci.* **2014**, *4*, 28–41. [CrossRef]
37. Sze, S.M.; Ng, K.K. *Physics of Semiconductor Devices*, 2nd ed.; John Wiley & Sons: New York, NY, USA, 1981; ISBN 0471143235.
38. Colinge, J.-P. *Silicon-on-Insulator Technology: Materials to VLSI*; Kluwer Academic Publishers: Boston, MA, USA, 2004; ISBN 9781402077739.
39. Colinge, J.P.; Gao, M.H.; Romano-Rodriguez, A.; Maes, H.; Claeys, C. Silicon-on-insulator 'gate-all-around device'. In Proceedings of the International Technical Digest on Electron Devices, San Francisco, CA, USA, 9–12 December 1990; pp. 595–598.
40. Reed, G.T.; Mashanovich, G.Z.; Gardes, F.Y.; Nedeljkovic, M.; Hu, Y.; Thomson, D.J.; Li, K.; Wilson, P.R.; Chen, S.W.; Hsu, S.S. Recent breakthroughs in carrier depletion based silicon optical modulators. *Nanophotonics* **2014**, *3*, 229–245. [CrossRef]
41. Aamer, M.; Thomson, D.J.; Gutiérrez, A.M.; Brimont, A.; Gardes, F.Y.; Reed, G.T.; Fedeli, J.M.; Hakansson, A.; Sanchis, P. 10 Gbit/s error-free DPSK modulation using a push-pull dual-drive silicon modulator. *Opt. Commun.* **2013**, *304*, 107–110. [CrossRef]
42. Lumerical's Tools Enable the Design of Photonic Components, Circuits, and Systems. Available online: https://www.lumerical.com/ (accessed on 1 June 2019).
43. Horikawa, T.; Shimura, D.; Mogami, T. Low-loss silicon wire waveguides for optical integrated circuits. *MRS Commun.* **2016**, *6*, 9–15. [CrossRef]
44. Zhang, Y.; Yang, S.; Lim, A.E.-J.; Lo, G.-Q.; Galland, C.; Baehr-Jones, T.; Hochberg, M. A compact and low loss Y-junction for submicron silicon waveguide. *Opt. Express* **2013**, *21*, 1310. [CrossRef]
45. Sze, S.M.; Ng, K.K. *Physics of Semiconductor Devices*; John Wiley & Sons: Hoboken, NJ, USA, 2006; ISBN 9780470068328.
46. Keil, U.D.; Liu, A.; Hodge, D.; Rubin, D.; Samara-Rubio, D.; Franck, T.; Liao, L.; Morse, M. High speed silicon Mach-Zehnder modulator. *Opt. Express* **2005**, *13*, 3129.

47. Green, W.M.; Rooks, M.J.; Sekaric, L.; Vlasov, Y.A. Ultra-compact, low RF power, 10 Gb/s silicon Mach-Zehnder modulator. *Opt. Express* **2007**, *15*, 17106. [CrossRef]
48. Thomson, D.J.; Gardes, F.Y.; Hu, Y.; Mashanovich, G.; Fournier, M.; Grosse, P.; Fedeli, J.-M.; Reed, G.T. High contrast 40Gbit/s optical modulation in silicon. *Opt. Express* **2011**, *19*, 11507. [CrossRef] [PubMed]
49. Baehr-Jones, T.; Ding, R.; Liu, Y.; Ayazi, A.; Pinguet, T.; Harris, N.C.; Streshinsky, M.; Lee, P.; Zhang, Y.; Lim, A.E.-J.; et al. Ultralow drive voltage silicon traveling-wave modulator. *Opt. Express* **2012**, *20*, 12014–12020. [CrossRef] [PubMed]
50. Debnath, K.; Thomson, D.J.; Zhang, W.; Khokhar, A.Z.; Littlejohns, C.; Byers, J.; Mastronardi, L.; Husain, M.K.; Ibukuro, K.; Gardes, F.Y.; et al. All-silicon carrier accumulation modulator based on a lateral metal-oxide-semiconductor capacitor. *Photonics Res.* **2018**, *6*, 373. [CrossRef]
51. Giguere, S.R.; Friedman, L.; Soref, R.A.; Lorenzo, J.P. Simulation studies of silicon electro-optic waveguide devices. *J. Appl. Phys.* **1990**, *68*, 4964–4970. [CrossRef]
52. Rubin, D.; Nicolaescu, R.; Jones, R.; Paniccia, M.; Liu, A.; Cohen, O.; Liao, L.; Samara-Rubio, D. A high-speed silicon optical modulator based on a metal–oxide–semiconductor capacitor. *Nature* **2004**, *427*, 615–618.
53. Samara-Rubio, D.; Liao, L.L.L.; Liu, A.L.A.; Jones, R.; Paniccia, M.; Cohen, O.; Rubin, D. A gigahertz silicon-on-insulator Mach-Zehnder modulator. In Proceedings of the Optical Fiber Communication Conference, 2004. OFC 2004, Los Angeles, CA, USA, 23–27 February 2004; Volume 2, pp. 7–9.
54. Kajikawa, K.; Tabei, T.; Sunami, H. An infrared silicon optical modulator of metal-oxide-semiconductor capacitor based on accumulation-carrier absorption. *Jpn. J. Appl. Phys.* **2009**, *48*, 4–8. [CrossRef]
55. Fujikata, J.; Takahashi, S.; Takahashi, M.; Horikawa, T. High speed and highly efficient Si optical modulator with MOS junction for 1.55 μm and 1.3 μm wavelengths. In Proceedings of the 10th International Conference on Group IV Photonics, Seoul, Korea, 28–30 August 2013; Volume 4, pp. 65–66.
56. Fujikata, J.; Noguchi, M.; Miura, M.; Takahashi, M.; Takahashi, S.; Horikawa, T.; Urino, Y.; Nakamura, T.; Arakawa, Y. High performance PIN Ge photodetector and Si optical modulator with MOS junction for photonics-electronics convergence system. In Proceedings of the 2013 18th Asia and South Pacific Design Automation Conference (ASP-DAC), Yokohama, Japan, 22–25 January 2013; pp. 655–656.
57. Perez-Galacho, D.; Abraham, A.; Olivier, S.; Vivien, L.; Marris-Morini, D. Silicon modulator based on interleaved capacitors in subwavelength grating waveguides. *Silicon Photonics Photonic Integr. Circuits V* **2016**, *9891*, 989112.
58. Liao, L.; Liu, A.; Rubin, D.; Basak, J.; Chetrit, Y.; Nguyen, H.; Cohen, R.; Izhaky, N.; Paniccia, M. 40Gbit/s silicon optical modulator for high-speed applications. *Electron. Lett.* **2007**, *43*, 1196–1197. [CrossRef]
59. Gardes, F.Y.; Thomson, D.J.; Emerson, N.G.; Reed, G.T. 40 Gb/s silicon photonics modulator for TE and TM polarisations. *Opt. Express* **2011**, *19*, 11804. [CrossRef]
60. Brimont, A.; Thomson, D.J.; Gardes, F.Y.; Fedeli, J.M.; Reed, G.T.; Martí, J.; Sanchis, P. High-contrast 40 Gb/s operation of a 500 μm long silicon carrier-depletion slow wave modulator. *Opt. Lett.* **2012**, *37*, 3504. [CrossRef]
61. Xiao, X.; Xu, H.; Li, X.; Li, Z.; Chu, T.; Yu, Y.; Yu, J. High-speed, low-loss silicon Mach–Zehnder modulators with doping optimization. *Opt. Express* **2013**, *21*, 4116. [CrossRef] [PubMed]
62. Gad, M.; Ackert, J.; Yevick, D.; Chrostowski, L.; Jessop, P.E. Ring Resonator Wavelength Division Multiplexing Interleaver. *J. Lightwave Technol.* **2011**, *29*, 2102–2108. [CrossRef]